Nuclear Science and Techniques (2023) 34:174
https://doi.org/10.1007/s41365-023-01322-z

ID effects on beam dynamics in the SSRF-U storage ring

Li-Yuan Tan[1,2] · Shun-Qiang Tian[1,3] · Xin-Zhong Liu[3] · Xu Wu[3] · Wen-Zhi Zhang[1,3]

Received: 28 February 2023 / Revised: 11 July 2023 / Accepted: 14 July 2023 / Published online: 21 November 2023

Abstract
This paper introduces the proposed insertion device (ID) scheme for the Shanghai Synchrotron Radiation Facility Upgrade. Based on this scheme, the influences of the ID radiation on the intra-beam scattering emittance and energy spread were evaluated. Optical distortion caused by the IDs was comprehensively examined and compensated using both local and global corrections. Subsequently, a frequency map analysis method was used to identify potentially dangerous resonance lines. In addition, the dynamic aperture, energy acceptance, and Touschek lifetime were calculated after considering high-order magnetic field errors to ensure that the ID effect did not affect the operation of the storage ring.

Keywords SSRF-U · Insertion devices · Emittance · Beam dynamic

1 Introduction

The Shanghai Synchrotron Radiation Facility [1, 2] devised an upgrade plan (SSRF-U) that aims to reach the soft X-ray diffraction limit [3, 4]. The SSRF-U plans to install numerous insertion devices (IDs) to provide a superior light source for additional beamline users. Compared to third-generation light sources, these IDs, which feature smaller magnetic gaps and higher magnetic fields, exert a greater influence on beam dynamics.

The ID effect on beam dynamics primarily manifests in three aspects: radiation, closed orbits, and optics. First, owing to the high magnetic field, the ID radiation losses are equivalent to or exceed those in the bending magnets. This resulted in a significant reduction in the equilibrium emittance and Touschek lifetime. Furthermore, independent adjustments of the ID field by beamline users may induce non-negligible fluctuations in beam parameters such as emittance and energy spread, potentially affecting photon brightness or distribution stability. These fluctuations may affect some sensitive beamline techniques such as microfocus beamlines, scanning transmission X-ray microscopy [5], and other experimental methods [6–8]. Second, ID mounting and magnetic field integral errors can lead to closed-orbit distortion (COD), which necessitates feedforward compensation using trim coils on both sides of the ID. Even in an ideal planar horizontal wiggler, the fringe field focusing of each pole can induce vertical focusing and distort the vertical beta function. This optical distortion breaks the lattice periodicity, excites previously insignificant resonance lines, generates new higher-order resonance lines, and degrades the dynamic aperture and momentum acceptance, decreasing the injection efficiency and beam lifetime. Therefore, it is essential to examine the effect of IDs on the beam dynamics in the SSRF-U.

Several methods have been proposed to compensate for the effects of the IDs. To address the effect of IDs on emittance, effective approaches include installing a fixed-gap wiggler in a variable dispersion bump [9], adjusting the variable-gap wiggler based on a feedback system with real-time monitoring [10], and optimizing the dispersion in straight sections [11]. To investigate the necessity of emittance compensation in the SSRF-U, we conducted a detailed analysis of the ID radiation effect in the following research. These findings demonstrate that the intra-beam scattering (IBS) effect significantly dilutes emittance fluctuations, thereby making emittance compensation unnecessary.

✉ Shun-Qiang Tian
tiansq@sari.ac.cn

[1] Shanghai Institute of Applied Physics, Chinese Academy of Sciences, Shanghai 201800, China

[2] University of Chinese Academy of Sciences, Beijing 100049, China

[3] Shanghai Advanced Research Institute, Chinese Academy of Sciences, Shanghai 201204, China

A feedforward system based on response-matrix measurements can effectively compensate for closed-orbit distortions, optical distortions, tune shifts [12], and coupling distortions [13, 14]. Shimming with permanent magnet shims or active shim wires is also an effective way to decrease the field integrals and phase errors in APPLE-II-type IDs [15, 16]. In addition, global compensation for closed orbits and optics can be achieved using the Linear Optics from Closed Orbits (LOCO) method [17]. Beta-beating is widely used to quantify the effect of IDs on optics. Analysis of IDs in the SSRF-U reveals that elliptically polarized undulators (EPUs) and superconducting wiggler (SCW) require local compensation, whereas the other IDs exert a minor influence and only require global compensation.

In this study, the kick map method [18] was used to evaluate the effect of IDs on closed orbits and optics. The kick map tables were generated by the symplectic integrator method [19] in the ELEGANT [20] software and then imported into the AT [21] software for particle tracking. The ID radiation and dispersion were not included in the kick map model. If these elements need to be calculated, effective approaches include either slicing the ideal planar ID into a combination of bending magnets or manually incorporating the radiation into the calculation formula.

This study focused on the effect of IDs on the SSRF-U storage ring. In Sect. 2, we briefly introduce basic information about the lattice and ID schemes. Section 3 studies the variations in emittance and energy spread caused by ID radiation effects, considers the IBS effect, and discusses the necessity for emittance compensation in the SSRF-U. In Sect. 4, we evaluate the optical distortion and tune shift using local and global compensation methods to restore the optics. Section 5 presents the frequency map analysis (FMA) results of the ID effect on the oscillation detuning and dynamic apertures, comparing the lattice include all IDs with that include all IDs and high-order magnet errors. The energy acceptance and Touschek lifetimes were also examined after considering the influence of the ID effect and magnet errors. Finally, we conclude the paper in Sect. 6.

2 Descriptions of the SSRF-U

The lattice of the SSRF-U storage ring consists of 20 × 7BA cells with a circumference of 432 m. This section presents the basics of the SSRF-U and briefly describes the ID scheme.

The main parameters of the bare lattice are summarized in Table 1 and the beam optics within a super period are shown in Fig. 1. Four straight sections with a length of 10.1 m were set up separately, two of which were used for the beam injection and high-frequency systems; only the other two sections were available for ID installation. The length of the standard straight section was 5.1 m, which was suitable for the current ID configuration of the SSRF. Each short straight section can accommodate two

Table 1 Main parameters of bare lattice and straight sections in SSRF-U storage ring

Parameters		Value
Lattice		20 × 7BA
Electron energy (GeV)		3
Circumference (m)		432
Average current (mA)		500
Tune (H, V)		51.17,16.22
Corrected chromaticity (H, V)		3,3
Natural bunch length (mm)		2.6
RF voltage (kV)		2000
RF frequency (MHz)		499.65
Harmonic number		720
Energy loss per turn (keV)		637.128
Natural energy spread		0.001351
Natural emittance (pm·rad)		53.2
Straight section		
Short	β_x (m)	5.05
	β_y (m)	2.99
Long	β_x (m)	15.25
	β_y (m)	5.69

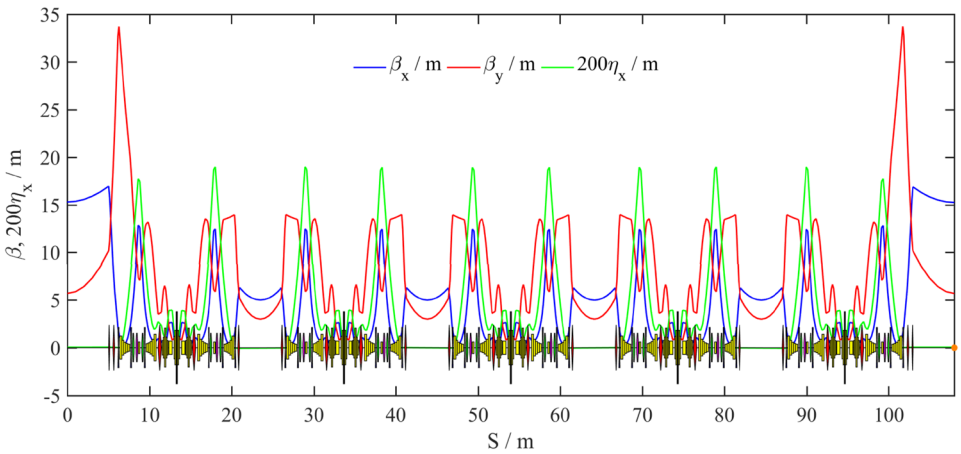

Fig. 1 (Color online) Beam optics in a super period of the SSRF-U storage ring

IDs with a length of approximately 2 m or one ID with a length of approximately 4 m. The maximum value of the dispersion function, approximately 0.095 m, occurred in the optical hump section, whereas the dispersion in the straight sections was negligible. An additional quadrupole was added on both sides of the long straight section to amplify the beta function at the injection point, thereby appropriately increasing the dynamic aperture in the x-direction while correspondingly decreasing it in the x'-direction. Consequently, ID perturbation in the long straight sections was much higher than that in the short straight sections. Moreover, the 2.1 T super bending magnet and 1.1 T dipoles in the arc section can also provide X-rays for beamline users. The total radiation loss per turn, calculated only for the dipoles and anti-bends, is 637.128 keV. However, this radiation loss almost doubled when the IDs were included. The natural beam emittance of 53.2 pm·rad reached the diffraction limit for soft X-rays. Nevertheless, the low emittance implies that the beam emittance affected by IBS will increase rapidly.

An insertion device scheme comprising 18 IDs was proposed to satisfy the requirements of different users. The ID parameters, including in-vacuum undulators (IVU), cryogenic permanent magnetic undulators (CPMU), wiggler (W), elliptically polarized undulator (EPU), and superconducting wiggler (SCW), are listed in Table 2. The short straight sections can only accommodate a 4 m ID and there are two additional quadrupole correctors on either side of the long straight sections. In the ensuing research, we assume that 2 EPUs are installed in the middle of the long straight sections, whereas the other IDs are installed in the middle of the short straight sections. In this scheme, although 18 IDs already occupy all the straight sections, the dual-canted-ID strategy [22] enables the installation of additional IDs by placing two IDs in the same straight section and providing beamlines for different users.

Table 2 Main parameters of insertion devices at SSRF-U

Type/name	λ_W (mm)	L_W(m)	$B^{max}(T)$
CPMU15×2	15	2	1
CPMU18×2	18	2	1.3
CPMU18×3	18	3.06	1.18
CPMU20×3	20	3.2	1.25
IVU20×2	20	2	1.16
IVU25×2	25	2	1.25
Wiggler80	80	2	1.43
EPU58	58	4	0.78
EPU148	148	4	0.69
SCW48	48	1.008	4.2

3 Radiation effects of the IDs

The ID radiation effect significantly increases the energy loss per turn, leading to higher radiation damping and lower natural emittance. The natural emittance and energy spread can be calculated using the synchrotron radiation integrals expressed in Eqs. (1) and (2), assuming that the ID optics effect is not considered.

$$\varepsilon_x = C_q \gamma^2 \frac{I_5}{I_2 - I_4}, \tag{1}$$

$$\sigma_E = \gamma \sqrt{\frac{C_q I_3}{2I_2 + I_4}}, \tag{2}$$

where γ is the relativistic energy, C_q equals 3.382×10^{-13} m and $I_2 - I_5$ are the radiation integrals expressed by:

$$
\begin{aligned}
I_2 &= \oint \frac{1}{\rho^2}\mathrm{d}s, \\
I_3 &= \oint \frac{1}{\rho^3}\mathrm{d}s, \\
I_4 &= \oint \frac{\eta}{\rho}\left(\frac{1}{\rho^2}+2k\right)\mathrm{d}s, \quad k=\frac{e}{P_0}\frac{\partial B_y}{\partial x} \\
I_5 &= \oint \frac{\mathcal{H}}{|\rho^3|}\mathrm{d}s, \quad \mathcal{H}_x = x\eta_x^2 + 2\alpha\eta_x\eta_x' + \beta_x\eta_x'^2.
\end{aligned}
\tag{3}
$$

The contribution of IDs to the emittance and energy spread can be described by their synchrotron radiation integrals when the ID is assumed to be a periodic magnet system. The complete expressions are given in Eq. (4) [23].

$$
\begin{aligned}
I_{2\mathrm{ID}} &= \frac{L_\mathrm{W}}{2\rho_\mathrm{W}^2} \\
I_{3\mathrm{ID}} &= \frac{4}{3\pi}\frac{L_\mathrm{W}}{\rho_\mathrm{W}^3} \\
I_{4\mathrm{ID}} &= -\frac{3}{32\pi^2}\frac{\lambda_\mathrm{W}^2}{\rho_\mathrm{W}^4}L_\mathrm{W} \\
I_{5\mathrm{ID}} &= \frac{\lambda_\mathrm{W}^4}{4\rho^4\rho_\mathrm{W}^5}\left[\frac{3}{5\pi}+\frac{3}{16}\right]\langle\gamma_x\rangle L_\mathrm{W} - \frac{9\lambda_\mathrm{W}^3}{40\pi^4\rho_\mathrm{W}^5}\langle\alpha_x\rangle L_\mathrm{W} + \frac{\lambda_\mathrm{W}^2}{15\pi^3\rho_\mathrm{W}^5}\langle\beta_x\rangle L_\mathrm{W}
\end{aligned}
\tag{4}
$$

Here, L_W represents the length of the insertion device, ρ_W denotes the radius of curvature associated with the effective magnetic field, λ_W signifies the period, and α_x, β_x, and γ_x are the Twiss parameter averages over the length of the device. In most cases, both the $I_{4\mathrm{ID}}$ equation and the first two terms of the $I_{5\mathrm{ID}}$ equation can be neglected, although they are not neglected in the following research. The ID radiation damping effect is included in the $I_{2\mathrm{ID}}$ equation and the quantum excitation effect caused by the dispersion contributed by the ID itself is included in the $I_{5\mathrm{ID}}$ equation.

To date, the natural emittance and energy spread have been calculated using synchrotron radiation integration with the given ID and ring parameters. In this approach, the contribution of optical distortion is ignored and we assume that both EPUs are in a horizontal linear polarization model and that the effective magnetic fields of all IDs are negligible at their maximum magnetic gaps. The ID parameters listed in Table 2 were sequentially incorporated into the synchrotron radiation integrals, and the calculated results are shown in Fig. 2. The results demonstrate the variation in the emittance and energy spread from the bare lattice (left) to the lattice with all IDs (right), while the ID gap is sequentially closed. Due to these variations, the horizontal emittance decreased from 53.2 to 43.6 pm·rad, along with a reduction in energy spread from 0.00134 to 0.00115. This decrease was due to the gradual increase in the radiation loss from the bare lattice (637 keV) to almost double (1185 keV) when all IDs were included. In addition, a sharp increase owing to the high-field SCW in both the emittance and energy spread can be observed at the rightmost point of Fig. 1. This phenomenon was due to the high quantum excitation associated with the large dispersion contributed by the SCW. When the contribution of the SCW was excluded, each general ID decreased the emittance by approximately 1.3% and the energy spread by 1.1%.

In future low-emittance storage rings, in which the electron density will be extremely high, there will be a high rate

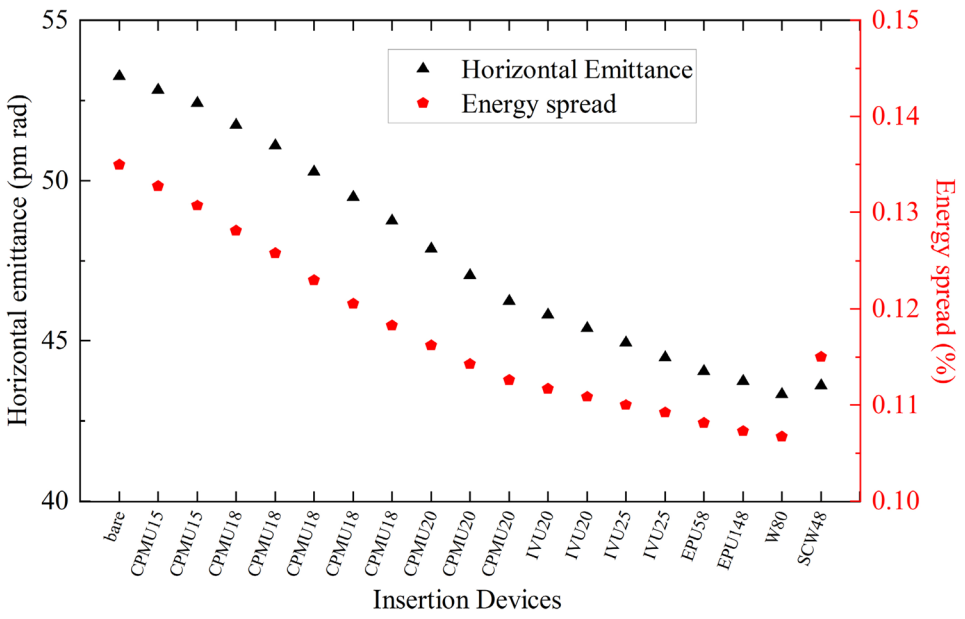

Fig. 2 Calculated emittance and energy spread by synchrotron radiation integrals in the SSRF-U with the insertion devices parameters listed in Table 2

of small-angle Coulomb scattering. This implies that the IBS effect may significantly impact the equilibrium emittance, energy spread, and bunch length of the new-generation light sources. A common strategy for mitigating the IBS effect is bunch lengthening using high-order harmonic cavities [24]. Simultaneously, it is also an effective way to reduce electron density by increasing transverse coupling.

In the subsequent study, after accounting for the ID radiation effect and disregarding the optical distortion, the Bjorken–Mtingwa model [25] was used to calculate the equilibrium IBS emittance and energy spread as a function of coupling, including no bunch lengthening, 3-factor, 5-factor, and 7-factor bunch lengthening. Figure 3 depicts the results for both the bare lattice and the lattice with all IDs, under fixed beam parameters of $I = 500$ mA, filling 500 bunches, and an RF frequency of 500 MHz. The dashed line represents the bare lattice, and the solid line corresponds to the lattice with all IDs. The area between the dashed and solid lines indicates the potential variation range induced by the IDs.

Compared with the result without the IBS effect shown in Fig. 2, the IBS equilibrium emittance increased by approximately 56% (without IDs) and 20% (with all IDs) in the case of the 100% beam coupling and 5-factor bunch lengthening, as depicted in Fig. 3. Simultaneously, the energy spread increased marginally. When comparing the results between the scenarios with no ID and with all IDs, after considering the IBS effect, the increase in transverse damping led to an emittance reduction of approximately 9 pm·rad for 100% beam coupling in 3-factor, 5-factor, and 7-factor bunch lengthening. The equilibrium IBS energy spread exhibited a substantial drop of approximately 25%. This phenomenon is caused by ID radiation, which is particularly significant in storage rings, where ID-induced radiation prevails over bending magnet radiation. In the SSRF-U, each ID decreased the emittance by 0.9% (with IBS), which was much less than the result without the IBS effect of 1.3%. This indicates that the IBS effect significantly diluted the emittance variation in the SSRF-U storage ring.

If the coupling is greater than 0.2, further increasing coupling has little influence on weakening the IBS effect. It can be observed that the effects of higher bunch lengthening and coupling gradually worsened. Additionally, it is worth noting that the dispersion contributed by ID itself was ignored in the kickmap model used in the above simulation results. Therefore, in the actual operation, the emittance will be marginally higher than the results shown in Fig. 3.

Upon analyzing the operational data from the current SSRF, we found that the variation in brightness was primarily attributed to EPUs [26]. Consequently, we focused on the IBS emittance and energy spread resulting from the EPUs (in the case of 5-factor lengthening and 20% beam coupling) and incorporated these factors into the SPECTRA software [27] to evaluate brightness variations in different beamlines. Table 3 presents the brilliance ranges of CPMU18, IVU20, and EPU58 for different harmonic numbers (1, 3, 5, 7, and 9), and the 2.1 T Super-B at different photon energies. The results indicate that the brilliance variation for each ID is approximately 0.5% (contributed by the EPUs), which does not affect beamline users during actual operation. Therefore, emittance variations do not cause significant instability in photon brightness or

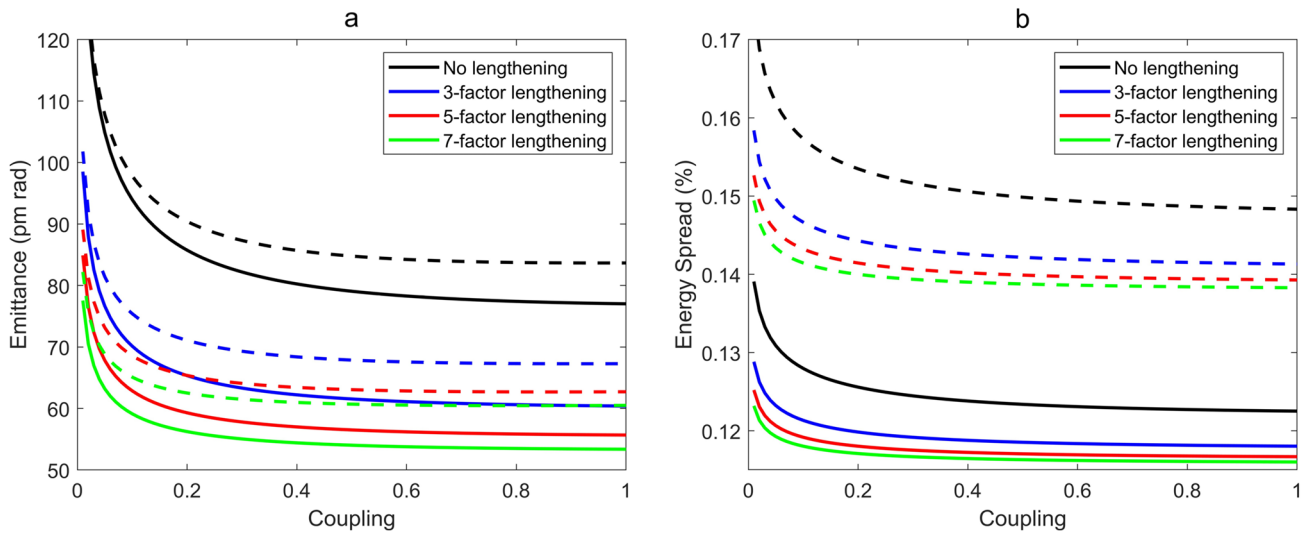

Fig. 3 (Color online) Equilibrium IBS emittance ($\varepsilon = \varepsilon_x + \varepsilon_y$) (**a**) and energy spread (**b**) as a function of coupling in 1, 3, 5, and 7 bunch-lengthening factors. The dashed line represents the bare lattice and the solid line the lattice with all IDs

Table 3 Brilliance (photons/sec/mm^2/mrad^2/0.1%B.W.) variation ranges of CPMU18, IVU20, EPU58 in different harmonic numbers and Super-B in different photon energies

Harmonic number	1	3	5	7	9
CPMU18 ($\times 10^{21}$)	4.364 ± 0.012	2.746 ± 0.008	1.640 ± 0.005	1.112 ± 0.003	0.8293 ± 0.0026
IVU20 ($\times 10^{21}$)	3.605 ± 0.009	2.388 ± 0.013	1.445 ± 0.004	0.9481 ± 0.0030	0.5475 ± 0.0017
EPU58 ($\times 10^{20}$)	5.786 ± 0.012	5.251 ± 0.013	3.252 ± 0.009	0.2548 ± 0.0007	0.1666 ± 0.0005
Energy (eV)	6	1000	5000	10000	50000
Super-B ($\times 10^{18}$)	0.295 ± 0.0008	0.416 ± 0.0012	1.015 ± 0.003	1.192 ± 0.0035	0.2041 ± 0.0006

distribution, which eliminates the need for emittance compensation in the SSRF-U storage ring.

4 Restoration of the beam optics distorted by the IDs

In this section, we focus on the ID effect on linear optics, which can be characterized by the root mean square (RMS) beta-beating ($\Delta\beta/\beta$) and RMS dispersion deviation ($\Delta\eta$). The EPUs and SCW, which caused significant optical distortion, were corrected locally, whereas the other IDs were corrected globally using the LOCO method.

Initially, we analyzed the optical distortion induced by the ideal periodic-field-insertion devices. The simulation results of the RMS beta-beating of the planar undulators and EPUs in the helical polarization operation model are shown in Fig. 4 as a function of the magnetic field intensity. The solid line represents the RMS beta-beating in the horizontal plane, and the dashed line indicates that in the vertical plane. As shown in the graph, the EPUs contribute approximately 6% to horizontal beta-beating, which is significantly higher than the 2% contributed to vertical beta-beating. The SCW had a 9% impact, exceeding that of the other planar undulators, which ranged from 1.5 to 3%. This substantial beta-beating highlights the necessity of establishing a local feedforward compensation system to mitigate the impact of the EPUs and SCW on linear optics.

Furthermore, we examined the impact of ID errors. The ID field integral and integral multipole errors were considered, as listed in Table 4. The IDs were modeled using kickmap slices owing to the periodicity of the ID magnetic field. Additional kick angles at the entrance and exit of the IDs were added to the ideal kick map table to simulate the field integral error, whereas the integral multipole errors were incorporated into each kick map slice. Subsequently, we used correctors located throughout the ring and the trim coils on both sides of the ID for orbit correction. In this section, we study only the closed-orbit distortion (COD) contributed by the IDs and consider a beam position monitor (BPM) measurement error of 0.2 μm. More complex error analysis was not the subject of this study; if needed, a first-turn simulation could be an effective method for further research [28]. A comparison of the COD before and after correction is shown in Fig. 5. Even when the ID field integral errors reach their maximum

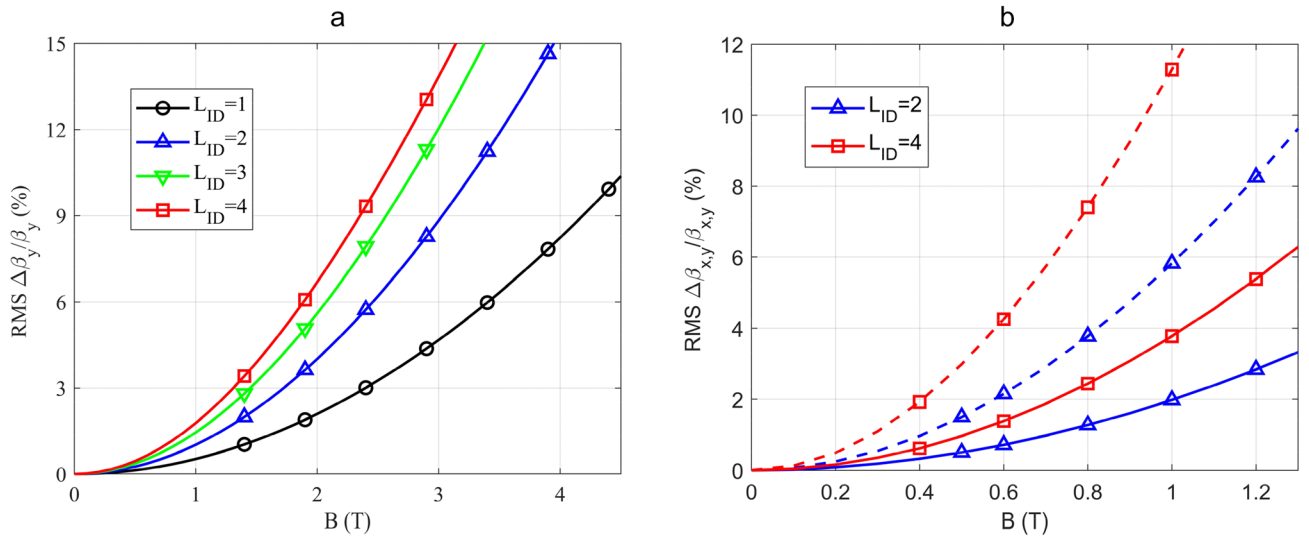

Fig. 4 RMS beta-beating as a function of ID field intensity. Planar undulators installed in short straight sections (**a**) and EPUs in helical polarization operation model installed in long straight sections (**b**). The solid line represents $RMS(\Delta\beta_x/\beta_x)$ and the dashed line $RMS(\Delta\beta_y/\beta_y)$

Table 4 ID field integral error and integral multipole error

	Value	
1st Int. Error	≤ 100 Gs · cm	
2nd Int. Error	≤ 10000 Gs · cm^2	
	Normal	Skew
Quad	≤ 50 Gs	≤ 50 Gs
Sex	≤ 50 Gs/cm	≤ 50 Gs/cm
Oct	≤ 50 Gs/cm^2	≤ 50 Gs/cm^2

values, the maximum kick angle for the feedforward coil is less than 1 μrad.

4.1 Local correction

As shown in Fig. 4, the EPUs and SCW have a significant influence on optics, which may significantly reduce the dynamic aperture, momentum acceptance, and Touschek lifetime. To mitigate the ID effect on beam dynamics, local compensation was built for these two EPUs and the SCW. By adjusting the quadrupoles nearest to the EPUs and SCW, this method facilitates the restoration of the optics and tunes the shift. The biggest advantage of this method is that the ID remains transparent to other areas after correction, even when beamline users adjust the ID magnet gap. In an actual operation, the feedforward table can be generated based on the measured response matrix of the corrector coils or nearest quadrupoles to restore closed-orbit distortion and optical distortion.

The compensation parameters for the quadrupoles were calculated using the optical and tune-shift matching methods. Twelve quadrupoles were located on both sides of the arc sections that could be adjusted to compensate for the two EPUs installed in the long straight sections. Additionally, 10 quadrupoles were available to compensate for the SCW installed in the short straight section.

Table 5 summarizes the results of the local correction for the EPUs and SCW, including the RMS beta-beating, RMS dispersion deviation, and tune shift, both before and after correction. As shown in the results, the remaining optical distortion for the EPUs was less than 0.4% in both the horizontal and vertical planes, and the tune shift was negligible. However, for the high-field SCW48, the optical distortion persisted at 0.67% in the horizontal plane and 1.32% in the vertical plane, even after the local optics correction. It should be noted that the local correction has a greater influence on dispersion, particularly in the horizontal plane. After local correction for EPUs and SCW, there was still an RMS beta-beating of 0.78% in the horizontal plane and 3.77% in the vertical plane, primarily attributable to the other IDs. Consequently, a global correction method is used in the following section to further reduce the optical distortion.

4.2 Global correction by the LOCO method

The LOCO method is a widely used technique for compensating global optics in particle accelerators. Based on the existing local compensation results, the LOCO method was used to correct the global optics and tune shifts by iteratively adjusting the quadrupole strengths. There are

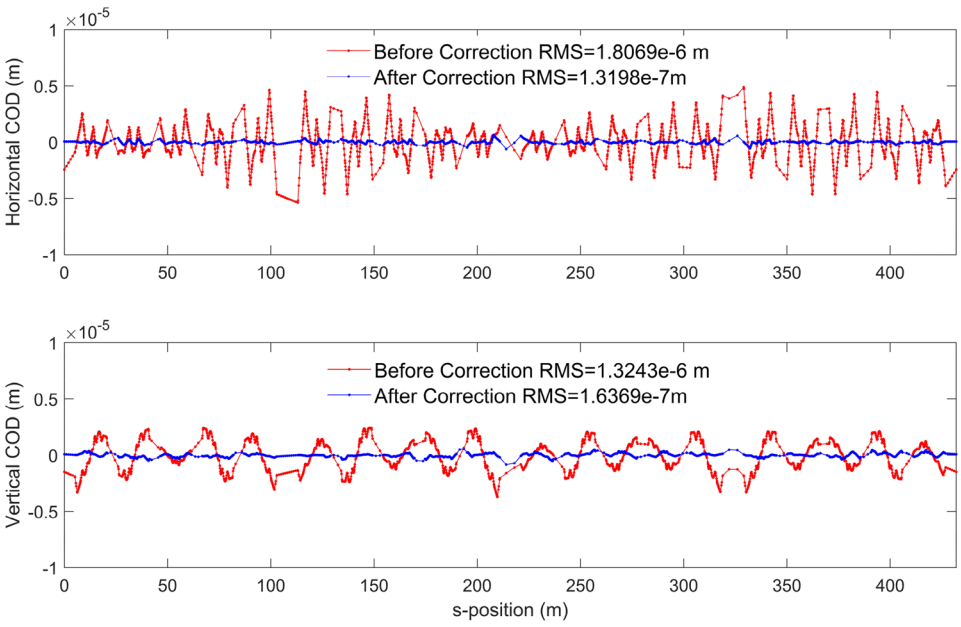

Fig. 5 (Color online) COD before and after correction in the horizontal and the vertical planes

240 beam position monitors (BPMs) and 208 quadrupole correctors on the ring that can be used for LOCO compensation and global tune-shift correction.

Figure 6 shows a comparison of beta-beating along the ring with all IDs before and after the LOCO correction in both the horizontal and vertical planes. Table 6 provides the metrics that describe the effect of the LOCO correction, including RMS beta-beating and RMS dispersion deviation; the tune shift after the LOCO correction can be neglected. As shown in Fig. 6, there is still a minor optical distortion near the IDs, especially near the high-field SCW. The residuals are mostly concentrated between the ends of the ID and the nearest quadrupole correctors. In addition to the horizontal distortion contributed by the EPUs, part of the horizontal distortion is produced when the quadrupole correctors are adjusted to compensate for the more substantial vertical distortion. As shown in Table 6, the residual of the RMS beta-beating is 0.77% in the horizontal plane and 2.39% in the vertical plane, which cannot be further reduced without additional correctors. Simultaneously, the RMS dispersion deviation after the LOCO correction is reduced to 0.05%. These factors can significantly affect the dynamic

Table 5 Impact of IDs on optics before and after local correction

	Before / After correction	$RMS(\Delta\beta_x/\beta_x)$ (%)	$RMS(\Delta\beta_y/\beta_y)$ (%)	$RMS(\Delta\eta_x)$ (%)	$RMS(\Delta\eta_y)$ (%)	$\Delta\nu_x,\ \Delta\nu_y$
EPU58	Before correction	6.94	2.28	0.0019	0.0002	0.0149,0.0053
	After correction	0.31	0.35	0.0861	0.0002	0,0
EPU148	Before correction	5.46	1.78	0.0047	0.0005	0.0118,0.0041
	After correction	0.24	0.27	0.0604	0.0006	0,0
SCW48	Before correction	0	9.12	0	0	0.0009,0.0205
	After correction	0.67	1.32	0.4061	0	0,0
All IDs	Before correction	5.65	10.42	0.0054	0.0006	0.0268,0.0985
	After correction	0.78	3.77	0.3230	0.0006	-0.0016,0.0687

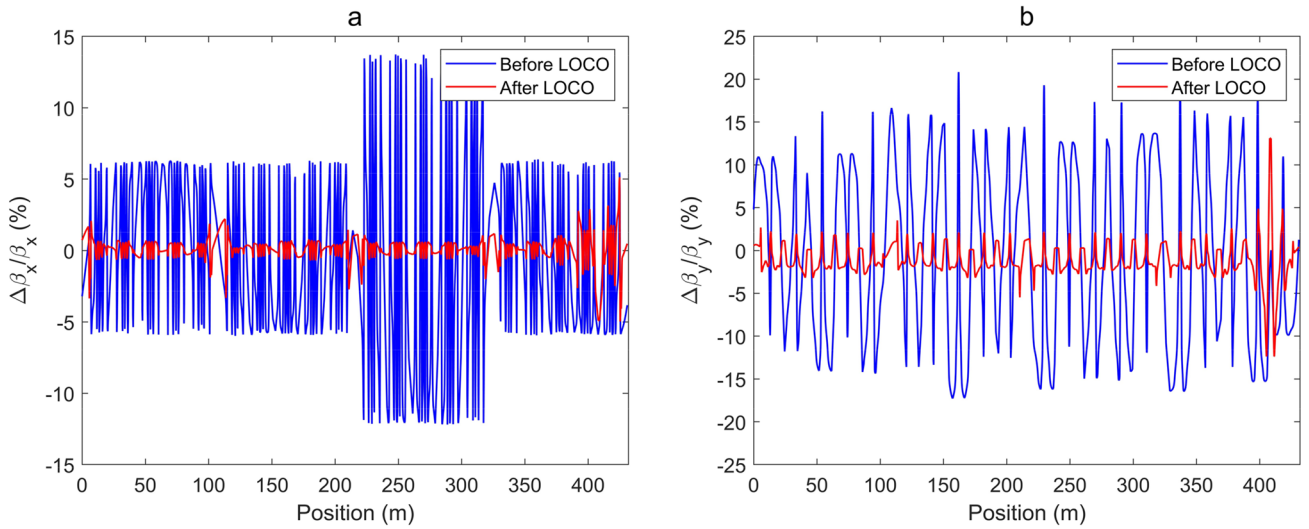

Fig. 6 (Color online) Horizontal and vertical beta-beating with all IDs without correction (**a**) and after LOCO correction (**b**)

Table 6 Impact of IDs on optics before and after global LOCO correction

	$RMS(\Delta\beta_x/\beta_x)$ (%)	$RMS(\Delta\beta_y/\beta_y)$ (%)	$RMS(\Delta\eta_x)$ (%)	$RMS(\Delta\eta_y)$ (%)
Without correction	5.65	10.42	0.0054	0.0006
After local correction	0.78	3.77	0.3230	0.0006
After global correction	0.77	2.39	0.0513	0.0543

aperture and momentum acceptance of the storage ring, which will be discussed in the following section.

5 Beam dynamics simulation

5.1 Oscillation detuning and dynamic apertures

In this section, we study the beam dynamics in the SSRF-U storage ring with all IDs after the LOCO correction. First, we discuss the dynamic aperture and nonlinear resonance caused by the IDs using FMA. Furthermore, to analyze whether the IDs affected the stable operation of the storage ring, the dynamic aperture, momentum acceptance, and beam lifetime were calculated after adding high-order magnetic field errors.

Figure 7 presents a comparison of the tune shifts between the bare lattice and the lattice with all IDs after the LOCO correction, along with the deviation in the oscillation amplitude. It can be seen that the tune shift is effectively adjusted by the LOCO correction. When the horizontal oscillation amplitude approaches –1, 1, –2, and 1.7 mm, the particle oscillation frequency approaches or crosses the resonance. This suggests that it is worth examining whether a small quadrupole field error in the storage ring can result in the loss of particles with larger amplitudes.

The nonlinear features of the SSRF-U storage ring detailed in this section were obtained from the simulation tracking of 2000 turns using the AT software. In addition to the FMA method, which uses four-dimensional particle tracking, the other simulations used six-dimensional particle tracking, encompassing both radiation loss and RF cavity.

Frequency map analysis (FMA) [29–31] is a powerful tool used in accelerator physics to assess the stability of particle motion and characterize the dynamic aperture and oscillation frequency around a closed orbit. Introduced in the early 1990s, FMA has been used extensively to analyze resonance structures within dynamic storage ring apertures. This tool helps us take measures to mitigate the presence of detrimental nonlinear resonances, which can affect the injection efficiency, beam lifetime, and overall operational performance. The FMA establishes a one-to-one mapping from action to angular frequency using tracking data to accurately calculate the frequency and its diffusion rate. The diffusion velocity is then used to illustrate the stability of the corresponding particle motion. FMA is effective for near-integrable systems with toroidal motions and helps avoid the occurrence of wide resonance, strong resonance, and resonance intersections by selecting an appropriate tune and chromaticity [32–34]. For simulation tracking to yield accurate results with the FMA, the radiation losses and energy compensation from the cavity must be removed.

The diffusion rate in tune space is defined by Eq. (5),

$$d_{\mathrm{r}} = \log_{10}\left(\frac{\sqrt{\Delta\nu_x^2+\Delta\nu_y^2}}{N}\right), \tag{5}$$

where the ν_x and ν_y are the transverse tunes, which are labeled on the color scale. Areas of instability are characterized by high diffusion rates with bright colors, and are usually related to the intersection of nearby resonance lines.

Figure 8 presents the frequency map graph of the SSRF-U storage ring, encompassing both the bare lattice and the lattice with all IDs after the LOCO correction. The color in the figure represents the difference between the particle

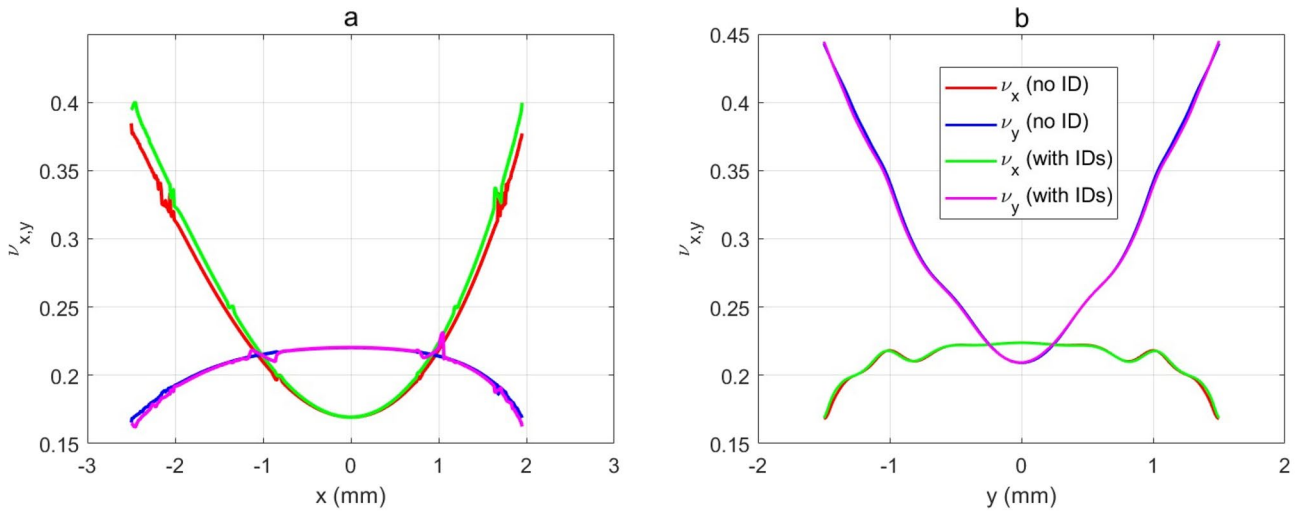

Fig. 7 (Color online) Fractional tune shifts with different amplitudes in the bare lattice and with all IDs after the LOCO correction in horizontal (**a**) and vertical (**b**) plane at the center of the long straight section

oscillation frequencies calculated using the tracking data from the first and last 1000 turns. The horizontal and vertical tunes were 51.17 and 16.22, respectively. Only a single third-order structural resonance was present in this region.

In the bare lattice (Fig. 8a, b), several "islands" are separated by resonance lines, especially the half-integer resonance and the structure resonance. The half-integer resonance $2Q_y = 33$ creates "islands" in regions with vertical amplitudes greater than 2 mm. The frequencies of particles with horizontal amplitudes of –2 and 1.7 mm lie on the third-order unstructured resonance line $3Q_x = 154$. Ideally, the particle motion is only slightly affected by this resonance. Within the dynamic aperture, no dangerous resonances exist except for some apparent resonance nodes. The third-order structure resonance $Q_x + 2Q_y = 4 \times 21$ has a significant effect on the dynamic aperture, separating the region at vertical amplitudes of approximately 1.5 mm. Although the dynamic aperture with radiation loss tracking does not identify the particle loss caused by this resonance, it is highly sensitive to magnetic field errors, which makes the resonance dangerous. In fact, particles are lost soon after entering the region owing to oscillation.

Figure 8c, d clearly shows that the optical distortion caused by the IDs disrupts the periodicity of the storage ring, significantly amplifies the third-order structure resonance line $Q_x + 2Q_y = 4 \times 21$, and excites numerous additional higher-order resonance lines. As illustrated in the frequency space of Fig. 8d, the most dangerous resonance line is $3Q_x = 154$, which restricts the dynamic aperture at $x = -2$ mm. This implies that if the optics distortion in the horizontal plane further increases, particles in the zone with x less than –2 mm will be entirely lost. More detailed

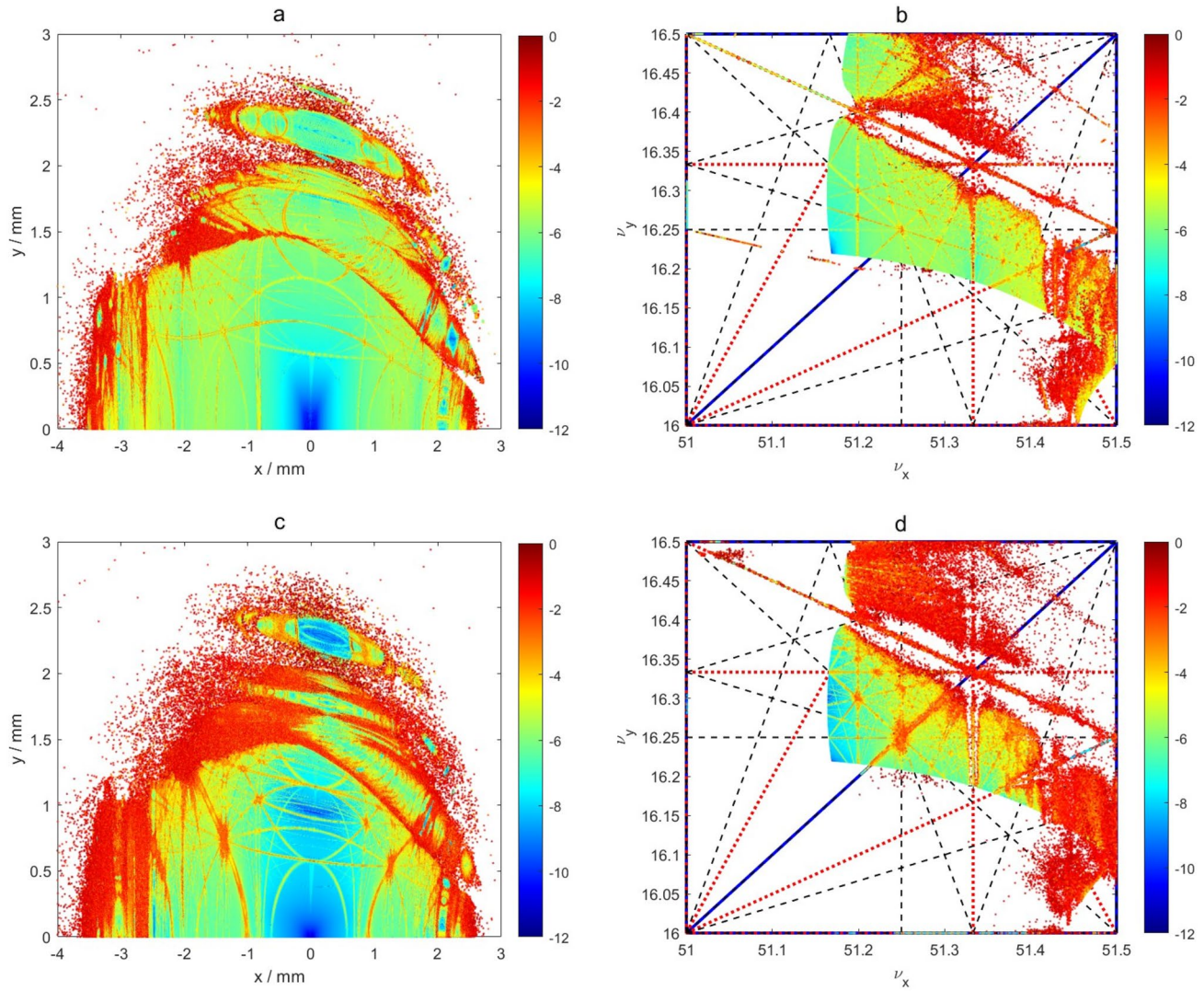

Fig. 8 (Color online) Dynamic aperture and frequency map analysis (FMA) results of both bare lattices (**a**, **b**) and with all IDs after LOCO correction (**c**, **d**)

simulation results in the SSRF-U have demonstrated that the threshold value of horizontal RMS beta-beating is approximately between 1 and 1.3%. If it exceeds 1%, the resonance line $3Q_x = 154$ will be significantly excited, rendering the vicinity of $x = -2$ mm unstable; if it surpasses 1.3%, the particles in the destabilized region will be entirely lost. Because the SWAPOUT injection is currently under preliminary consideration, as long as the effects of the IDs on the optics are properly compensated for, these effects should not significantly affect the SSRF-U injection.

In the ensuing research, 50 high-order magnetic field error seeds were added to the dipoles, quadrupoles, and sextuples, including the normal and skew errors, as listed in Table 7. Normal and skew errors were assigned the same amplitude. Based on the measurement data from the SSRF, the maximum amplitude of the intrinsic errors in the magnets was assumed to be 5×10^{-4}, while the non-intrinsic errors were presumed to have a maximum amplitude of 1×10^{-4}.

Table 7 Maximum amplitude value of high-order magnetic field error presented by $\Delta B/B$. Both the normal error and skew error were set with the same amplitude

Order	*RMS*($\Delta B/B$)		
	Dipole	Quad	Sex
3	5×10^{-4}	5×10^{-4}	0
4	1×10^{-4}	5×10^{-4}	5×10^{-4}
5	5×10^{-4}	5×10^{-4}	5×10^{-4}
6	1×10^{-4}	5×10^{-4}	5×10^{-4}
7	5×10^{-4}	1×10^{-4}	5×10^{-4}
8	1×10^{-4}	1×10^{-4}	5×10^{-4}
9	5×10^{-4}	1×10^{-4}	5×10^{-4}
10	1×10^{-4}	5×10^{-4}	1×10^{-4}

After adding the multipole errors, we first compared the optical distortion caused by the ID effects and multipole errors. The maximum RMS beta-beating contributed by the multipole errors was less than 0.015% in both the horizontal and vertical planes. In addition, the ID integral multipole errors were of the same order of magnitude. Therefore, compared with the optical distortion caused by the IDs, the errors contributed a small proportion.

Figure 9 illustrates the dynamic aperture at the center of the long straight section under different energy deviations $\Delta P/P$ (0, 1.5, and –1.5%), including the bare lattice and all IDs with 50 high-order magnetic field error seeds after the LOCO correction. The solid lines represent the median numbers of calculated data points. The figure shows that the dynamic aperture ($\Delta P/P = 0$) reduced less than 10% after adding all IDs when considering high-order magnetic field errors. Simultaneously, the dynamic aperture with a 1.5% energy deviation decreased slightly. Consequently, the ID effects and high-order magnetic errors will not significantly affect beam injection.

5.2 Energy acceptance and Touschek lifetime

The energy acceptance of a storage ring is determined by its nonlinear dynamics as well as the limitations imposed by the RF voltage and the size of its dynamic aperture. This parameter refers to the maximum energy deviation at which a particle remains stable while circulating within the ring. Energy acceptance, which is also affected by the dispersion

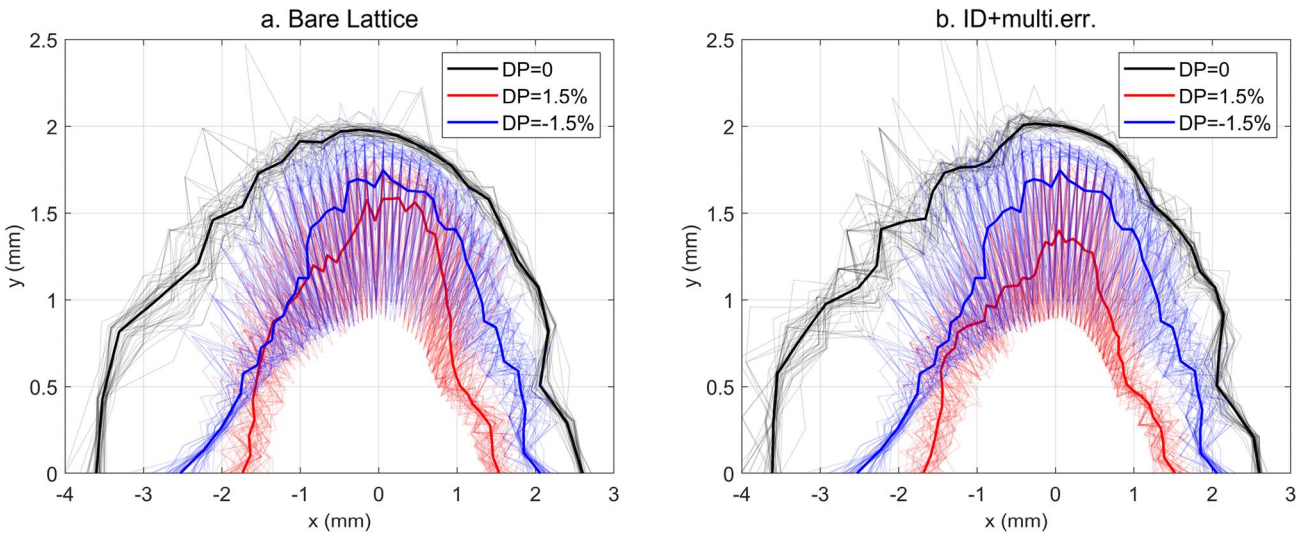

Fig. 9 (Color online) Dynamic aperture with 50 multipole error seeds in the bare lattice (**a**) and all IDs after the LOCO correction (**b**) in energy deviations $\Delta P/P = 0$, 1.5, and –1.5%. The solid lines represent the median numbers

function, tends to be smaller in areas where the dispersion is greater. Figure 10 shows the fractional tune shift with the deviation of the oscillation energy at the center of the long straight section. Particles with an energy deviation of –2.2% have already exceeded the half-integer resonance. Because the error considered was not very large, the particles were not lost when crossing the half-integer resonance [35].

Figure 11 shows the energy acceptance distribution of the storage ring for both the bare lattice and all IDs after considering magnetic errors. The figure was obtained by tracking each position according to the arrangement of the magnetic elements. The vacuum chamber was assumed to have a circular cross section with a radius of 10 mm, which represents the maximum amplitude of the particles during tracking.

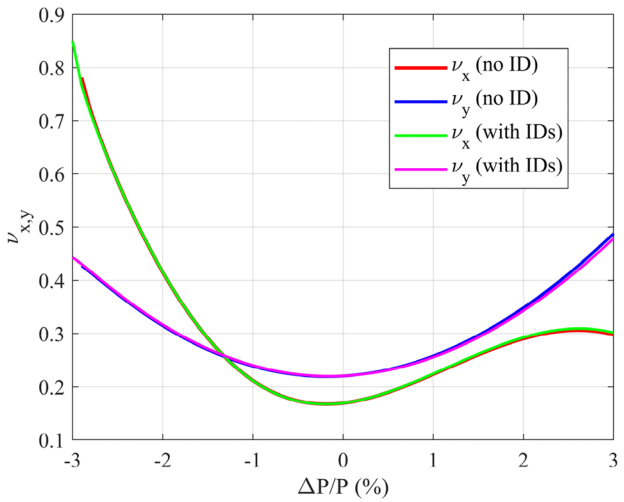

Fig. 10 (Color online) Fractional tune shift with the deviation of oscillation energy at the center of the long straight section

In the bare lattice, the energy acceptance in the long straight section exceeded ± 2.5% and the minimum value was approximately ± 1.5% in the arc section, effectively capturing the injected beam with energy dispersion. This energy acceptance ensures a substantial beam lifetime in the storage ring. However, after considering the IDs and multipole errors, Fig. 11 shows a notable reduction in the arc sections, particularly on the negative side. In the high-dispersion areas, where optical distortions were the most sensitive, the minimum value decreased from 1.5 to 1%. This reduction in energy acceptance is inevitable because of the existence of multipole errors and residual optics distortion after the LOCO correction.

The primary factor influencing beam lifetime is the Touschek lifetime, which results from electron Touschek scattering. Unlike multiple small-angle scatterings (intra-beam scattering) within a bunch, Touschek scattering constitutes a large-angle scattering process that transfers the transverse momentum of a particle to the longitudinal direction. If the energy deviation of a particle exceeds the acceptable energy, the particle is lost, thereby considerably reducing the beam lifetime. In this section, we discuss the Touschek lifetime with IDs after the LOCO correction in the SSRF-U storage ring. The Touschek lifetime was calculated using Eq. (6), as derived by Piwinsik [36]:

$$\frac{1}{\tau_{\text{Touschek}}} = \left\langle \frac{r_0^2 c N_b}{8\pi\gamma^2\sigma_s} F\left(\delta_m, B_1, B_2\right) \frac{1}{\sqrt{\sigma_x^2\sigma_y^2 - \sigma_\delta^4 D_x^2 D_y^2 \beta\delta_m}} \right\rangle. \tag{6}$$

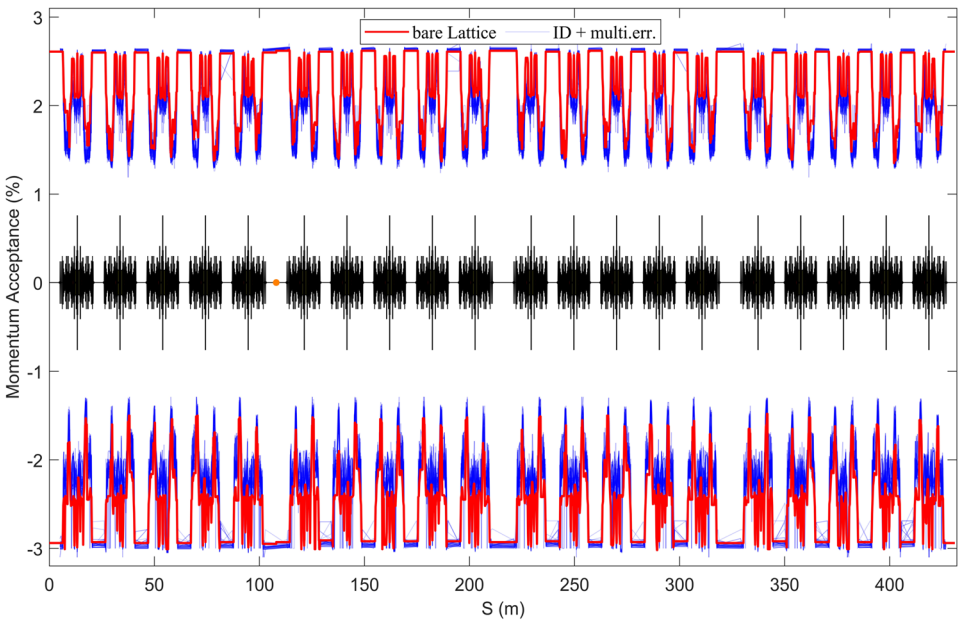

Fig. 11 (Color online) Energy acceptance in the bare lattice and with all IDs after the LOCO correction and multipole errors

In this equation, r_0 represents the classical electron radius, c denotes the speed of light in vacuum, N_b is the number of particles in each bunch, γ is the Lorentz factor, σ_s is the bunch length, δ_m is the momentum acceptance, σ_x and σ_y correspond to the transverse beam sizes, and F is a function of the Twiss parameter and momentum acceptance.

Equation (6) shows that the average Touschek lifetime is determined by the Twiss parameter, electron density, energy acceptance, and beam size. The Touschek lifetime is strongly dependent on the electron density and energy acceptance. However, both electron density and beam size are influenced by the IBS effect, whereas the Twiss parameter is associated with optics. To calculate the Touschek lifetime, we used the IBS results from Sect. 3, optics results after the LOCO correction (with errors) from Sect. 5.1, and momentum acceptance results from Sect. 5.2. These results were substituted into Eq. (6) to calculate the Touschek lifetime, as follows: similar to the IBS effect analysis, we considered bunch-lengthening factors of 1, 3, 5, and 7, under a beam current of 500 mA, filling 500 bunches, and an RF frequency of 500 MHz. The Touschek lifetime as a function of beam coupling with all IDs and multipole errors is shown in Fig. 12, where the solid lines represent the median number and the error bars represent the standard deviation.

The Touschek lifetime of the bare lattice is discussed in Ref. [3]. In the case of the 5-factor bunch lengthening and 20% coupling, the Touschek lifetime was approximately 3.1 h. However, after adding IDs and multipole errors, the Touschek lifetime significantly decreased to 1.07 ± 0.06 hours, as shown in Fig. 12. Two factors contributed to the substantial reduction in Touschek lifetime. First, the radiation damping contributed by the IDs reduces the IBS equilibrium emittance and energy spread, leading to a decreased bunch size and increased charge density. This triggered a considerable increase in the Touschek scattering rate, which primarily accounts for the deterioration in the beam lifetime. Second, multipole errors and residual optics distortions inevitably reduce the momentum acceptance. Increasing the bunch lengthening continues to be an effective method for enhancing Touschek lifetime. Additionally, if the coupling can be increased, the Touschek lifetime can be further improved.

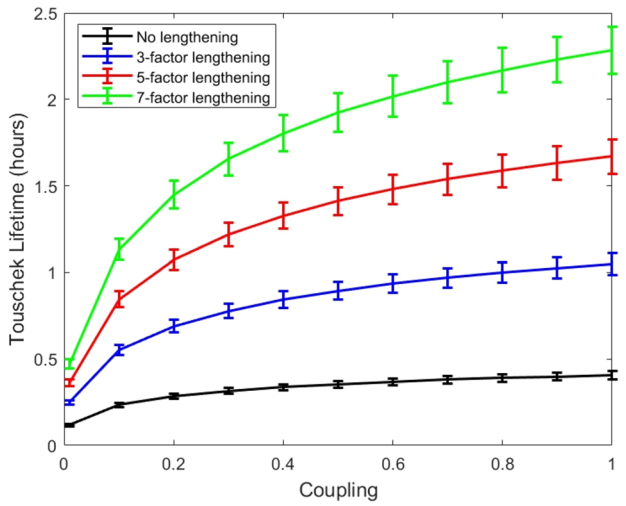

Fig. 12 (Color online) Touschek lifetime with all IDs after the LOCO correction with 50 multipole error seeds as a function of coupling in different bunch lengthening factors. The solid lines represent the median number and error bars represent the standard deviation

6 Conclusion

In this study, we present an overview of the SSRF-U storage ring and propose an ID scheme based on user requirements. The effects of ID radiation and optics on beam dynamics were calculated by incorporating the IBS effect. The results indicated that the average impact of each ID on the emittance was less than 1%. The RMS beta-beating contributed by the EPUs and SCW exceeded 5%, necessitating separate local compensation. Local and global compensation were used to restore the global optics and tunes. After the LOCO correction, the RMS beta-beating was reduced to 0.77% in the horizontal plane and 2.39% in the vertical plane. Subsequently, the dynamic aperture and nonlinear resonance were analyzed using the FMA method. The most dangerous resonance line, $3Q_x = 154$, was identified, which could restrict the horizontal oscillation amplitude to less than 2 mm if the horizontal optical distortion continued to increase. High-order magnetic field errors were also factored into the calculation, and the resulting dynamic aperture satisfied the requirements for transverse on-axis beam injection. The average energy acceptance can still ensure beam lifetime during high-current operation.

Author contributions All authors contributed to the study conception and design. Material preparation, data collection, and analysis were performed by Li-Yuan Tan, Shun-Qiang Tian, and Xin-Zhong Liu. The first draft of the manuscript was written by Li-Yuan Tan and all authors commented on previous versions of the manuscript. All authors read and approved the final manuscript.

Data availability The data that support the findings of this study are openly available in Science Data Bank at https://doi.org/10.57760/sciencedb.j00186.00088 and https://cstr.cn/31253.11.sciencedb.j00186.00088.

Declarations

Conflict of interest The authors declare that they have no competing interests.

References

1. H.J. Xu, Z.T. Zhao, Current status and progresses of SSRF project. Nucl. Sci. Tech. **19**, 1–6 (2008). https://doi.org/10.1016/S1001-8042(08)60013-5
2. X. Wu, S.Q. Tian, X.Z. Liu et al., Design and commissioning of the new SSRF storage ring lattice with asymmetric optics. Nucl. Instrum. Methods Phys. Res. A **1025**, 166098 (2022). https://doi.org/10.1016/j.nima.2021.166098
3. X.Z. Liu, S.Q. Tian, X. Wu et al., Intra-beam scattering and beam lifetime in a candidate lattice of the soft X-ray diffraction-limited storage ring for the upgraded SSRF. Nucl. Sci. Tech. **32**, 83 (2021). https://doi.org/10.1007/s41365-021-00913-y
4. Z.T. Zhao, L.X. Yin, Y.B. Leng et al., Consideration on the future major upgrades of the SSRF storage ring. in *Proceedings of IPAC2015, Richmond, VA, USA*. TUPJE023, pp. 1672–1674 (2015). https://doi.org/10.18429/JACoW-IPAC2015-TUPJE023
5. F. Sannibale, S.C. Leemann, H. Nishimura et al., Compensation of insertion device induced emittance variations in ultralow emittance storage rings. in *Proceedings of IPAC2018, Vancouver, BC, Canada*. WEXGBE2, pp. 1751–1754 (2018). https://doi.org/10.18429/JACoW-IPAC2018-WEXGBE2
6. H.T. Li, B. Zhao, X.Z. Zhang et al., Development of a portable laser heating device for synchrotron radiation in situ experiment. Nucl. Tech. **46**, 020101 (2023). https://doi.org/10.11889/j.0253-3219.2023.hjs.46.020101. (**in Chinese**)
7. H.Z. Liu, J. Li, S.Q. Gu et al., Upgrade of transmission XAFS data acquisition system upgrade of Shanghai Synchrotron Radiation Facility BL14W1 beamline station. Nucl. Tech. **45**, 070103 (2022). https://doi.org/10.11889/j.0253-3219.2022.hjs.45.070103. (**in Chinese**)
8. S.Q. Gu, B.B. Mei, Z. Jiang et al., Data acquisition system of a von Hamos X-ray emission spectrometer based on PILATUS detector. Nucl. Tech. **45**, 090101 (2022). https://doi.org/10.11889/j.0253-3219.2022.hjs.45.090101. (**in Chinese**)
9. F. Sannibale, M. Ehrlichman, T. Hellert et al., Compensation of insertion device induced emittance variations in ultralow emittance storage rings by a dispersion bump in a wiggler. in *Proceedings of IPAC2019, Melbourne, Australia*. TUPGW093, pp. 1627–1630 (2019). https://doi.org/10.18429/JACoW-IPAC2019-TUPGW093
10. D. Hidas, T. Shaftan, T. Tanabe, Emittance and energy spread compensation for current and future low emittance synchrotron light sources. Phys. Rev. Accel. Beams **24**, 081601 (2021). https://doi.org/10.1103/PhysRevAccelBeams.24.081601
11. T. Hiraiwa, K. Soutome, H. Tanaka, Suppression of emittance variation in extremely low emittance light source storage rings. Phys. Rev. Accel. Beams **25**, 040703 (2022). https://doi.org/10.1103/PhysRevAccelBeams.25.040703
12. Y.M. Zhou, X.Y. Xu, Y.B. Leng, Precise measurement and application of synchrotron tune at storage ring. Nucl. Tech. (in Chinese) **44**, 090103 (2021). https://doi.org/10.11889/j.0253-3219.2021.hjs.44.090103
13. X.Z. Liu, S.Q. Tian, X. Wu et al., Feedforward compensation of the insertion devices effects in the SSRF storage ring. Nucl. Sci. Tech. **33**, 70 (2022). https://doi.org/10.1007/s41365-022-01052-8
14. S.Q. Tian, G.M. Liu, W.Z. Zhang et al., Calibration of the linear optics in the SSRF storage ring. Nucl. Sci. Tech. **19**, 257–265 (2008). https://doi.org/10.1016/S1001-8042(09)60001-4
15. J. Bahrdt, W. Frentrup, A. Gaupp, et al., Shimming of the Dynamic field integrals of the BESSY II U115 hybrid undulator. In *Proceedings of IPAC2011*, San Sebastián, Spain. THPC154, pp. 3248–3250 (2011).
16. B. Singh, R. Bartolini, R. Fielder et al. Active shimming of dynamic multipoles of an APPLE II undulator in the DIAMOND storage ring. In *Proceedings of IPAC2013, Shanghai, China*. TUPWO057, pp. 1997–1999 (2013).
17. J. Safranek, Experimental determination of storage ring optics using orbit response measurements. Nucl. Instrum. Methods Phys. Res. A **388**, 27–36 (1997). https://doi.org/10.1016/S0168-9002(97)00309-4
18. P. Elleaume, A new approach to the electron beam dynamics in undulators and wigglers. in *Proceedings of EPAC1992*, Berlin, Germany, pp. 661–664 (1992).
19. Y.K. Wu, E. Forest, D.S. Robin, Explicit symplectic integrator for s-dependent static magnetic field. Phys. Rev. E **68**, 046502 (2003). https://doi.org/10.1103/PhysRevE.68.046502
20. M. Borland, ELEGANT: A flexible SDDS-compliant code for accelerator simulation. Argonne National Lab., USA (2000). https://doi.org/10.2172/761286
21. A. Terebilo, Accelerator toolbox for MATLAB, SLAC National Accelerator Lab., Menlo Park, CA, USA (2001). https://doi.org/10.2172/784910
22. P.K. Den Hartog, G.A. Decher, L.J. Emery, Dual canted undulators at the advanced photon source. in: Proc. PAC03, Portland, Oregon U.S.A. MPPB004, pp. 833–835 (2003).
23. A. Ropert, High brilliance lattices and the effects of insertion devices. CERN, pp. 158–194 (1990). https://doi.org/10.5170/CERN-1990-003.158
24. Z.G. Zhang, Y.B. Zhao, K. Xu et al., Low level radio frequency controller for superconducting third harmonic cavity at SSRF. Nucl. Tech. **45**, 120101 (2022). https://doi.org/10.11889/j.0253-3219.2022.hjs.45.120101(inChinese)
25. J.D. Bjorken, S.K. Mtingwa, Intrabeam scattering. Part. Accel. **13**, 115–143 (1983)
26. L.Y. Tan, S.Q. Tian, X.Z. Liu et al., Emittance and energy spread compensation in future synchrotron light sources. Nucl. Instrum. Methods Phys. Res. A **1052**, 168278 (2023). https://doi.org/10.1016/j.nima.2023.168278
27. T. Tanaka, H. Kitamura, SPECTRA: a synchrotron radiation calculation code. J. Sync. Radiat. **8**, 1221–1228 (2001)
28. B. Wang, Y. L. Zhao, Z. Duan et al., Progress of the first-turn commission simulations for HEPS, in *Proceedings of IPAC2021*, Campinas, SP, Brazil, TUPAB008, pp. 1349–1351 (2021).
29. H.S. Dumas, J. Laskar, Global dynamics and long-time stability in Hamiltonian systems via numerical frequency analysis. Phys. Rev. Lett. **70**, 2975 (1993). https://doi.org/10.1103/PhysRevLett.70.2975
30. D. Robin, C. Steier, J. Laskar et al., Global dynamics of the Advanced Light Source revealed through experimental frequency map analysis. Phys. Rev. Lett. **85**, 558 (2000). https://doi.org/10.1103/PhysRevLett.85.558
31. J. Laskar, Frequency map analysis and particle accelerators. in *Proceedings of PAC2003*, Portland, Oregon, USA, pp. 378–382 (2003). https://doi.org/10.1109/PAC.2003.1288929
32. S.Q. Tian, G.M. Liu, H.H. Li et al., Nonlinear optimization of the modern synchrotron radiation storage ring based on frequency map analysis. Chin. Phys. C **33**, 127 (2009). https://doi.org/10.1088/1674-1137/33/2/011
33. S.Q. Tian, G.M. Liu, H.H. Li et al., Tune optimization of the third-generation light source storage ring based on Frequency Map Analysis. Chin. Phys. C **33**, 224 (2009). https://doi.org/10.1088/1674-1137/33/3/012
34. Y. Jiao, S.X. Fang, Q. Qin et al., Tune optimization of modern light sources. Nucl. Instrum. Methods Phys. Res. A **566**, 270–280 (2006). https://doi.org/10.1016/j.nima.2006.07.056
35. Y. Jiao, Z. Duan, Statistical analysis of the limitation of half integer resonances on the available momentum acceptance of the High

Energy Photon Source. Nucl. Instrum. Methods Phys. Res. A **841**, 97–103 (2017). https://doi.org/10.1016/j.nima.2016.10.037
36. A. Piwinski, *The Touschek Effect in Strong Focusing Storage Rings*. Cern Library Record (1999). https://arxiv.org/pdf/physics/9903034.pdf